Fish-ridge wind turbine aerodynamics characteristics in Oscillating Water Column (OWC) system

by Nurul Hiron

Fish-ridge wind turbine aerodynamics characteristics in Oscillating Water Column (OWC) system

Nurul Hiron[*1,2], Ida A.D. Giriantari[2a], Lie Jasa[2b] and I. Nyoman S. Kumara[2c]

[1]Department of Electrical Engineering, University of Siliwangi, Jl Siliwangi 24, Tasikmalaya, Indonesia
[2]Department of Electrical Engineering, University of Udayana, PB. Sudirman, Bali, Indonesia

Abstract.   This paper analyzes the fish-ridge type wind turbine performance and characteristics of energy extraction applied in a low wave Oscillating Water Column (OWC) system. This article contributes to providing a better understanding of the application of OWC and VAWT in a low wave environment. The aerodynamic characteristics of the three-blade fish-ridge turbine in an OWC chamber have been successfully investigated. CFD simulation with Reynolds-Averaged-Stokes (RANS) equations was used to obtain airspeed and air pressure contours under compressed and decompressed conditions in the turbine blades. Experiments on laboratory scale test rig also obtained data. The blade torque and turbine power coefficient at different AoA were validated through the experimental test to obtain numerical equations for the relationship between airspeeds, torque, tip speed ratio, and turbine power. The turbine design was 0.2 m long and 0.1 m wide and with an overlap ratio of 15%. The maximum tested airspeed was 20m/s. We found that the fish-ridge turbine has a homogeneous air velocity distribution and pressure due to the 15% overlap area. The maximum efficiency of the fish-ridge turbine under compressed conditions was 30% at TSR 0.9, while under decompressed conditions, the maximum efficiency reached 28% at TSR 0.6.

Keywords: wind energy; wind turbine; oscillating water column; CFD; dynamic wind effects; pressure distribution; RANS equations; Navier-Stokes equations

1. Introduction

In a system with oscillating water column (OWC) technology, turbines play an essential role in converting ocean wave energy into electrical energy. We believe that the ocean is an unlimited natural resource (Hiron *et al.* 2019). Turbine performance measures are generally seen from the power coefficient (CP) (Kavade and Ghanegaonkar 2020) and the torque coefficient (CT). The higher the CP value, the better the turbine efficiency. Several aerodynamic resistance factors influence the Vertical Wind Axis Turbine (VAWT) efficiency. They are the number of blades, weight of the material, and distribution of airspeeds required of the turbine blade. Generally, the turbine's efficiency is between 20% and 30% (Sobczak *et al.* 2020).

VAWT applied in an OWC system has been used to extract low wind speeds (Lipian *et al.* 2020). The VAWT generally has a maximum CP at TSR = 0.8 to 1.02 (Bachtiar 2019) (Yao *et al.* 2019), (Chen *et al.* 2016), which means it works at low airspeeds, while Horizontal Wind Axis Turbine (HAWT) are generally designed for high airspeeds (Matoug *et al.* 2020).

A two-blade Savonius-type VAWT in an e OWC system at low waves yielded CP=20%, while a fish-ridge turbine in an OWC system resulted in CP = 24.5% (Hiron *et al.* 2019). Therefore, many researchers have proposed different designs so that the CP can exceed 20%.

The works reported in this paper investigate a fish-ridge turbine performance based on the turbine model proposed by Song *et al.* (2013). The focus of observations is on the aerodynamic characteristics of the turbines under compressed and decompressed conditions in an OWC system. There is little information regarding this area in the literature. The parameters observed are CP (Lipian *et al.* 2020), torque coefficient (CT) (Agbormbai and Zhu 2020), turbine rotation (rpm), wind power, and turbine power against the angle of attack (AOA). Here, we propose a modified turbine fish-ridge with an overlap ratio (OR) of 15%. This turbine design associated with turbine design from (Song *et al.* 2013), (Chao *et al.* 2017) uses an OR of 29.8%, which in our opinion, the better OR for savonius is between 10% - 16% as shown by Bachtiat (2019) and (Chen *et al.* 2016).

Overlap on turbine blades affects the performance of the turbine. The test results prove that an overlap of 10% -16% produces the best performance (Bachtiar 2019), while inside (Hassanzadeh and Mohammadnejad 2019) has confirmed that 20% overlap makes the best performance; this is also the same as savonius with three blades (Morshed *et al.* 2019). Therefore in this article, the overlap is set at 15%.

Song *et al.* (2013) first introduced the fish-ridge turbine. According to Song, the ideal blade shape for a fish-ridge turbine is a chord length value of 18% of the initial design value, the radius of curvature is 4% of the initial design value, and the stagger angle is 23% of the original design (Song *et al.* 2013). In 2015, Song continued his research, comparing the fish-ridge performance with savonius in an open spaces environment (Song *et al.* 2015). The results showed the fish-ridge turbine had a higher power coefficient than the savonius. The fish-ridge turbine produced higher power and higher torque coefficient. It was 7% greater than the savonius at an airspeed of 10m/s. Several studies related to VAWT performance can be seen in Table 1.

The implementation of the fish-ridge type VAWT turbine in the OWC system provides novelty in energy diversification research. So far, studies on fish-ridge have only been carried out in open spaces (Chao *et al.* 2017), (Hassanzadeh and Mohammadnejad 2019),(Chao *et al.* 2017). In an OWC system, two different conditions occur alternately for rotating the turbine. They are-compressed-and-decompressed conditions. The compressed condition is when the water level rises, thus creating high air pressure in the turbine chamber. The decompressed condition is when the water level drops, creating a state for decompressed in the air space. Both the compressed and decompressed conditions generate/cause high airflow, thus turning the turbine.

This article presents a detailed analysis based on works that have been carried out on the fish-ridge turbine as reported by Song (2013), Hiron *et al.* (2019), Chao *et al.* (2017), Hassanzadeh (Hassanzadeh and Mohammadnejad 2019), and Chao *et al.* (2017). The aerodynamic phenomenon of the airflow inside the OWC with a fish-ridge turbine is simulated using ANSYS to produces parameters of the generated wind power and the static torque to AoA of the turbine so that the fish-ridge work on the OWC system can be explained in more detail. The analysis is carried out on the upstream speed variations in the OWC chamber, namely 6m/s, 10m/s, and 14m/s. Static torque is carried out at one full rotation at angle of 0 degrees to 360 degrees. A CFD simulations uses Reynolds-Aaveraged Navier – Stokes (RANS) equations (Muneer *et al.* 2015), (Yang *et al.* 2021) to

Table 1 Previous research on three-blade and two-blade savonius

Blade number	Cp	TSR	OR	Author
3	31%	1.02	10%	(Bachtiar 2019)
3	23%	0.8	15%	(Chen *et al.* 2016)
3	22.8%	0.9	15%	(Yao *et al.* 2019)
3	30%	0.8	15%	(Sobczak *et al.* 2020)
2	21%	0.8	10%	(Hassanzadeh and Mohammadnejad 2019)
2	35%	0.8	16%	(Chen *et al.* 2016)
2	24.5%	0.45	15%	(Hiron *et al.* 2019)

obtain detailed data related to free-stream velocity and air pressure dynamics on the turbine surface. We compared the CFD results and the lab-scale prototype experiment data to validate the fish-ridge static torque analysis.

2. Research method

The static torque of the turbine uses two approaches. The first test is based on CFD. The second is based on the prototype measurements using a digital torque meter and anemometer with a data logger, as shown in Fig. 8. The program is ANSYS version 18.2. The equation on the relationship between turbine rpm and airspeeds at OWC is obtained through prototype measurements is shown in Fig. 8. The CP value against TSR can be calculated using Eq. (5). The modification parameters of the fish-ridge turbine are suggested in Table 2.

The fish-ridge turbine performance analysis is conducted based on simulation in two conditions. They are in compressed and decompressed states. The position of the turbine blade in the direction of wind flow is divided into four angles, at 72 degrees, 60 degrees, 30 degrees, and 0 degrees. The simulation results show airspeeds contours and air pressure under compressed and decompressed conditions. The methods are as follows:

2.1 Fish-ridge turbine

The fish-ridge rotor model used in this research is modified from the savonius blade reported by Song *et al.* (2013). The fish-ridge turbine design is based on the curvature of the fish-ridge fish-ridge. The goal is to reduce aerodynamic drag on the turbine blades. In work reported by Song et al. (Song *et al.* 2015), they studied the fish-ridge with savonius in an open-air environment. It was found, at an airspeed of 10 m/s, the fish-ridge efficiency can be reached 24.22% and 18.52% for the savonius turbine (Chao *et al.* 2017).

The turbine fish-ridge design is shown in Fig.1. The property of the fish-ridge turbine consists of large radius arcs (R2). The value of R2 is determined using Eq. (3). The other parameters are the radius of small arcs (R1), turbine diameter (D), stagger angle of small-arcs (α), stagger angle of large-arcs (β), diameter axis (d), diameter overlap (S), and chord length (L). Based on Chao *et al.* (Chao *et al.* 2017), the curvature of fish-ridge blades in computational form is represented by Eq. (1), where constanta ψ =0.977 and constanta $\xi = 0.8719$. The distance between the blades is 120 degrees, using Eq. (2), then the total angles of α_1 and α_2 must be 120 degrees. The overlap ratio
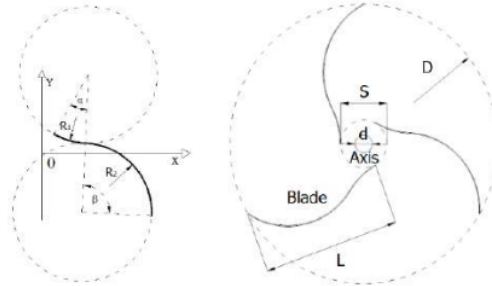
Fig. 1 Design of radius of curvature and small arc fish-ridge (Chao *et al*. 2017)

(OR) is determined using Eq. (4). From these provisions, it forms a fish-ridge turbine blade formation as shown in Fig. 1.

$$y(x,t) = (\psi x + \xi x^2)\sin(1.2516 + 1.4924) \tag{1}$$

$$\alpha_1 + \alpha_2 \approx 120^0 \tag{2}$$

$$R = \frac{D}{2} \times \tan 30° \tag{3}$$

$$OR = (S - d)/L \tag{4}$$

2.2 Oscillating water column mechanism

Fig. 2 shows the working system mechanism of an OWC that we proposed, and as an affirmation, we give a border as the scope of the study in this article. In simple terms, OWC converts ocean wave energy into kinetic energy based on the oscillations that occur in the chamber. Our observation area is the turbine working environment in the chamber, as shown in Fig. 2.
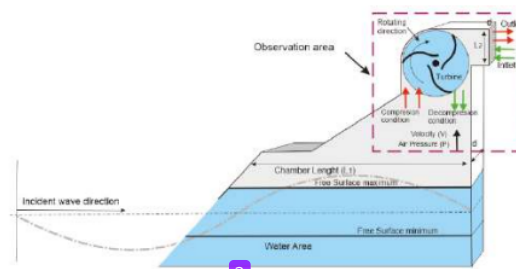

Fig. 2 The mechanism of the OWC with a fish-ridge turbine

An illustration of the implementation of OWC as part of a sea wave power plant using a wind turbine is shown in pada Fig. 3. We designed the OWC building to be placed long away on the coastal area, especially beaches threatened with abrasion by sea waves. The OWC design that we present has multi-functions, including a power generator; OWC can become seawall for coastal conservation solution.

Koefisien torque Static and coefficient Power of turbine

Turbine performance is generally determined from two main variables, namely CP and CT. CP stated that the turbine efficiency in extracting the energy received from the energy produced is in the form of mechanical energy (Kavade and Ghanegaonkar 2020). Therefore, The CP is expressed as Eq. (5), which is the ratio between the turbine power (PT) and the airspeeds. The airspeed power is the multiplication of the constant value=0.5. The air density (ρ) is in kg/m3, and the swept area of the turbine (A) is in m² and the airspeeds (V) in m/s. The value of PT can be obtained from the multiplication of the turbine torque (TT) in N.m against the turbine shaft rotation (ωT) in rad/s. PT can also be obtained through CFD simulations.

The turbine efficiency based on torque extraction is calculated using Eq. (7). The TS is the torque produced by the turbine in N.m, and R is the turbine radius in meters.

$$Cp = \frac{P_T}{0.5 \ \rho A V^3} \tag{5}$$

$$P_T = \ T_T x \omega_T \ (watt) \tag{6}$$

$$C_T = \frac{T_T}{0.5 \ \rho A R V^2} \tag{7}$$

$$C_T = \frac{T_T}{0.5 \ \rho A R V^2} \tag{8}$$

2.3 Turbine geometry

The fish-ridge turbine is designed with three blades, following a design (Chao *et al.* 2017). The fish-ridge blade formation is based on the parameters shown in Fig. 1, where the blade curve geometric shape is based on Eq. (1). We modify it at OR = 15%. Details and differences in turbine parameters are presented in Table 2.
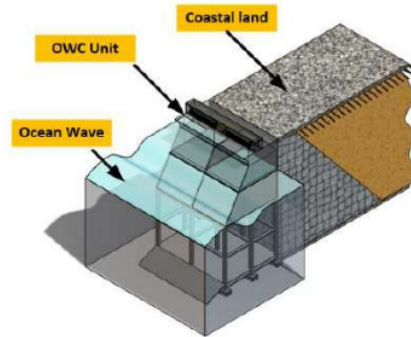

Fig. 3 The Illustration of OWC implementation as a low-wave power plant

Table 2 Turbine parameter comparison

Geometrical Parameters	Symbols	Dimension	
		Proposed	Song *et al.**, Chao *et al*
Height turbine	H	200 mm	700 mm
Diameter turbine	D	100 mm	700 mm
radius of curvature	R	27.8 mm	192.5 mm
stagger angle	α	10.110	10.11°
chord length	L	55,2 mm	386 mm
small arc	Lm	17 mm	30 mm
Diameter axis	d	14.5 mm	45 mm
Diameter overlap	S	22.8 mm	160 mm
The angle of the large circular	α_1	850	910
Overlap ratio (OR)	α_2	350	270
	OR	15%	29.8%

* (Chao *et al.* 2017), (Song *et al.* 2013)

(a)   (b)
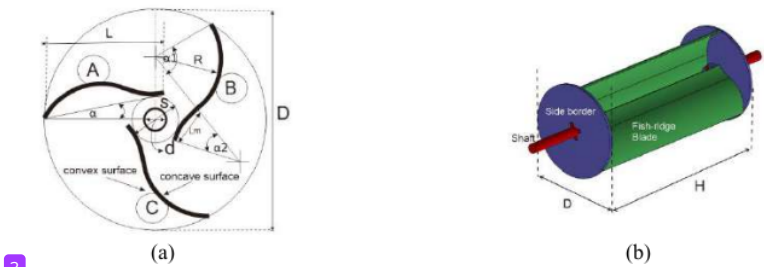
Fig. 4 The design of the fish-ridge turbine. (a). The side view of the fish-ridge turbine with overlap ratio (OR) and (b). Fish-ridge turbine 3D design

The turbine prototype and model used in CFD follow the basic design as shown in Fig. 4. To identify the AoA angle, we give the initials blade (A), blade (B), and blade (C) as shown in (Fig. 4(a)). Each blade has a 120 degrees angle to the other blade. Fish-ridge turbine 3D design with the initials D as the diameter (m) of the turbine and H as the turbine length in meter (Fig. 4(b)).

2.4 Domain meshing

The boundary domain of the fish-ridge turbine model consists of the rotating and stationary zones. The rotating zone is a vertical cylindrical shape with a position in the middle plane. The stationary zones are the part that supports the turbine, as shown in Fig. 5. The boundary domain consists of inlet and outlet velocities, as shown in Fig. 6. The inlet velocity is where the air flows into the turbine. The outlet is the place where air flows out of the turbine.
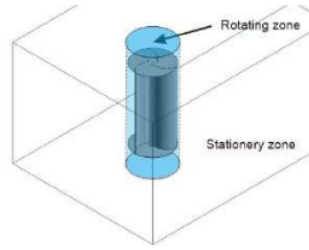
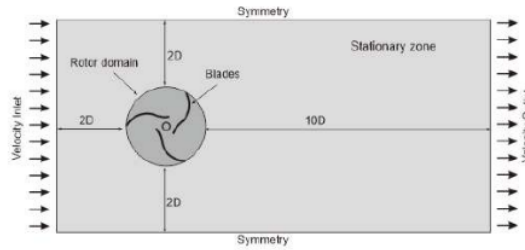Fig. 5 Rotating and stationary zones in isometric view

Fig. 6 Computational domain scheme

The meshing model uses a maximum size of 0.08 mm across all domains. A hexahedral meshing is chosen to obtain a high computational resolution in the computational process to form airspeeds and air pressure contours. In contrast, around turbine blades, a tetrahedral meshing type is used to solve the complex geometry around the surface of the turbine blades.

Torsion testing on the simulation experiment is carried out at airspeeds of up to 20 m/s. The prototype static torque measurement is measured using a torque meter model HNJ-1 equipped with a data logger. Turbine torque is measured at an AoA angle from 0 degrees to 360 degrees.

Analysis of airflow dynamics in a VAWT turbine is based on the linear potential theory described by Kang *et al.* (2018). The Reynolds-Averaged Navier – Stokes (RANS) equations (Langer and Swanson 2020). RANS involves continuity equations, momentum equations, and energy equations as governing equations form (Kang *et al.* 2018). The turbulent model is needed to solve the closure of the regulatory equation. However, the suitability of the turbulence model is still a matter of debate. The turbulence model of the Spalart-Allmaras equation was chosen to describe the complex flow of the turbine rotor (Rahman 2020). In general terms, the Navier – Stokes equation is expressed as follows

$$\rho \frac{\partial U_i}{\partial t} + \rho U_j \frac{\partial (U_i U_j)}{\partial x_j} = -\frac{\partial p}{\partial x_i} + \frac{\partial}{\partial x_j}\left(\frac{\partial U_i}{\partial x_j} + \frac{\partial U_j}{\partial x_i} \right) \tag{9}$$

$$\rho \frac{\partial U_i}{\partial t} + \rho U_j \frac{\partial U_i}{\partial x_j} = -\frac{\partial p}{\partial x_i} + \frac{\partial}{\partial x_j}\left(\left(\frac{\partial U_i}{\partial x_j} + \frac{\partial U_j}{\partial x_i} \right) - \rho \overline{\acute{\mu}_j \acute{\mu}_i} \right) \tag{10}$$

3. Results and discussions

3.1 Static torque with CFD

The CFD simulation was applied to obtain the static turbine torque. The numerical approach was used based on Navier – Stokes, as Eqs. (9) and (10) as presented in Table 3. In the simulation model, the turbine blades are given the initial A, B, C to indicate the position of the blades concerning AoA. Observations were made on blade C because blade C is the blade positioned behind the wind direction, so blade C is the blade that gets the minor drag power from the wind.

Table 3 shows the distribution of airflow in fish-ridge turbines based on variations in the AoA angle. Using CFD simulation, the air distribution in the turbine shows different airflow dynamics based on variations in the AoA angle. The observation area is an image with a red circle. The simulation is displayed in the form of zoom-out for the simulation area, and zoom-in only shows the observation area.

The simulation results of observations from Table 3 can be described as follow:

1. AoA = 0 degree, the wind flow appears to hit the concave plane of blade B. Large circular and small circular play a role in distributing the thrust of downstream wind flow in a laminar form from blades B and A to the concave plane of blade C. then, downstream flow forms a vortex flow on blade C. This downstream flow then provides thrust support on blade C to contribute to an even distribution of airspeed in each blade.

2. At AoA = 20 degrees, it appears that there is a continuous flow of air on blade C so that at an angle of AoA=20 degrees, it can be concluded that there is no significant aerodynamic resistance. No 3 shows the continuation of the wind flow that occurs in No 2. At AoA = 40 degrees, it appears that there is an increase in airflow in the C blade due to OR, so that at the angle AoA = 400, it can be concluded that there is no significant aerodynamic resistance.

3. At AoA = 40 degrees, the airspeeds flowing in the OR become more solid than in No 1, 2, 3.

4. AoA=60 degrees is the angle where the OR inlet space faces the wind accident, which then causes the wind flow to accelerate on the C blade. This condition proves that the curvature of the fish-ridge blades allows the wind flow to be more easily distributed than conventional savonius turbines.

5. AoA=80 degrees, the high airspeeds in the OR area causes blade C to get high thrust, even though blade B still occurs slowly due to aerodynamic drag from blade A, but blade C provides considerable power compensation.

6. AoA=100 degrees. There is low airspeed distribution between blade B and blade C. Even though there is high flow in the OR area. The aerodynamic resistance on blades B and C is lacking.

From the description of Table 3, it can be concluded that OR=15 contributes to the thrust of the blade, which indirectly gets the thrust from the incoming wind. These results prove the facts from a study conducted by (Shamsoddin and Porté-Agel 2020).

We present the static torque test results on the turbine rotor rotation at airspeeds of 5m/s. However, we have managed to collect static torque data against AoA at several turbine rpm, which varies from 7.5 rpm to 120 rpm, as shown in Fig. 7. This analysis can conclude that the more rotation of the turbine, the smaller the torque produced. The turbine rotor rotation at low speed (15 rpm) has the highest torque of 0.00686 N.m. the average torque obtained by the maximum value is 0.044 occurs at AoA 10 degrees, 120 degrees, 250 degrees.

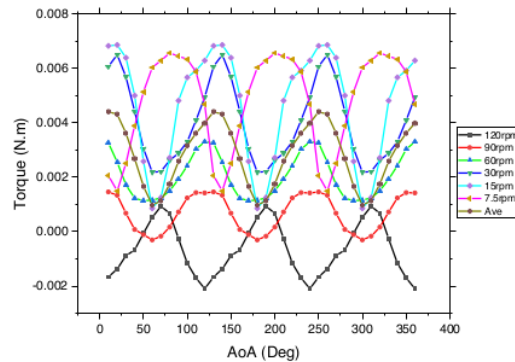Table 3 The contour of air distribution in fish-ridge turbine

No	Observation area in Zoom out	Observation area in Zoom in
1		
2		
3		
4		
5		
6		
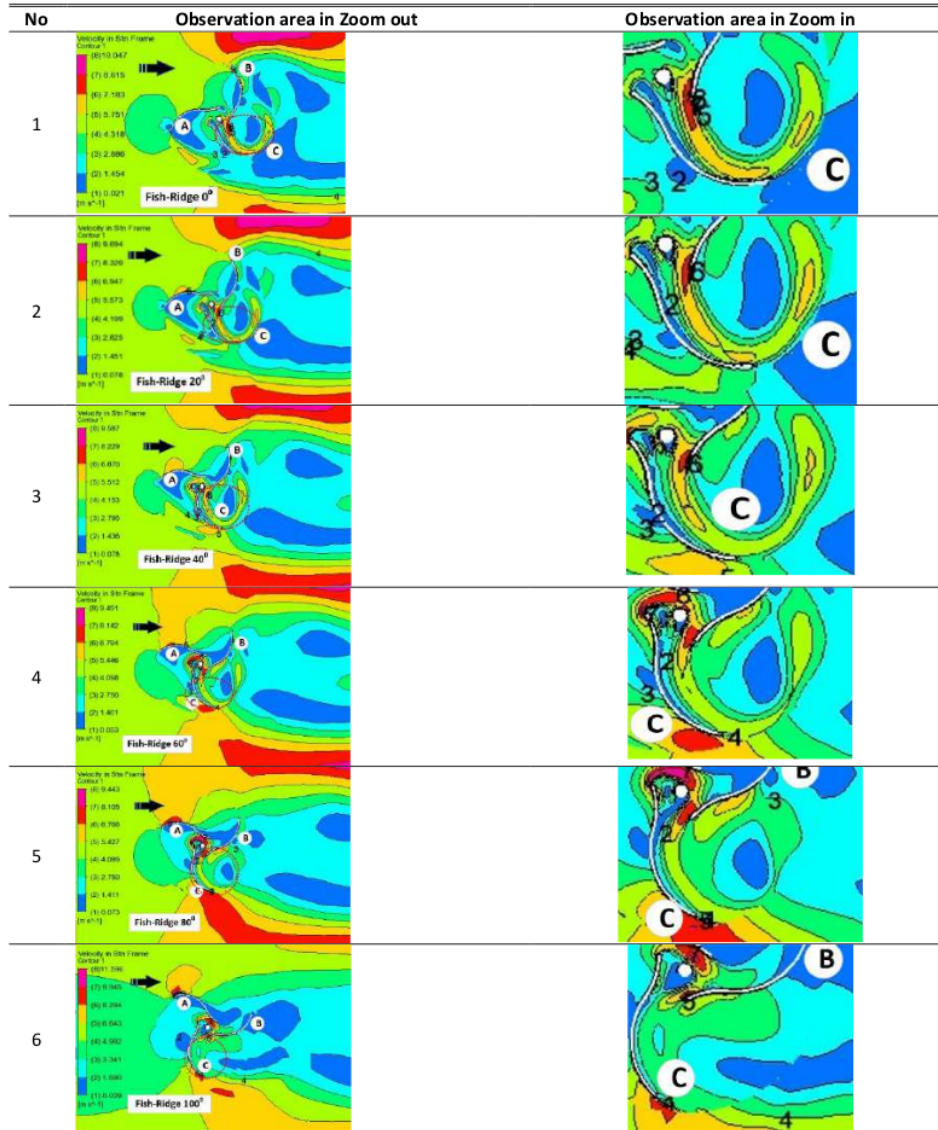
Fig. 7 Static torque vs. AoA at various rpm

Table 4 Peak torque at various turbine rotation

Rotation (RPM)	AoA (Degrees)		
7.5	80	200	320
120	70	190	310
15	20	140	260
30	20	140	260
90	10	130	250
60	120	240	360

Fig. 7 also shows that fish-ridge turbines at high rpm appear to reduce torque, creating negative torque. The torque reduction is because, at high speeds with low airspeeds, fish-ridge turbines experience decreased performance. This condition is a weakness of the commonly encountered VAWT turbines. by previous researchers.

Static torque testing of variations in turbine rotor rotation is concluded in Table 4, and the AoA= 10 degrees to 20 degrees occurs a rotation at 15 rpm, 30 rpm, and 90 rpm. The AoA=70 degrees to 80 degrees occurs at rotation 7.5 and 120 rpm. The AoA=120 degrees occurs at a rotation of 60 rpm.

3.2 Static torque with prototype experiment

We were also testing the prototype turbine on the experimental as in Fig. 8. The airspeeds towards the turbine are set at 5 m/s. The results of the mean torque measurement of five repetitions are shown in Fig. 9. Then it is compared with the simulation results at the mean torque of Fig. 7.

Comparison of static torque observations based on the simulation against the prototype measurement as in Fig. 9 shows that the two tests show that the maximum torque occurs at AoA 80

degrees, 200 degrees, and 320 degrees. The result is that our prototype produces 0.007 Nm of torque while the simulation, the turbine, produces 0.078 Nm.

From the static torque test, it can be concluded that the fish-ridge turbine has a high response at low airspeeds; therefore, the fish-ridge turbine is very suitable for use in low-wave OWC systems. Using the mean torque value from Fig. 7, then numerically through the curve fitting as in Eq. (11), shows relationship between the airspeeds and the torque generated by the fish-ridge turbine Fig. 10. TR is the turbine rotor torque (N.m), WS is the airspeeds (m/s).

$$T_R = -0.0005 \ (W_S) + \ 0.0054 \tag{11}$$

The relationship of TSR to fish-ridge turbine torque can be calculated numerically using Eq. (12), where TR is the turbine rotor torque (N.m), constanta, and constanta. TSR is obtained using Eq. (8). The graph of the TSR relationship to turbine torque is shown in Fig. 11.

$$T_R = \Pi(TSR^2) \ + \Psi \ (TSR) \ + \ 0.00543 \tag{12}$$
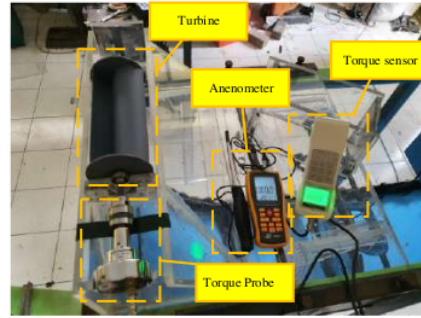
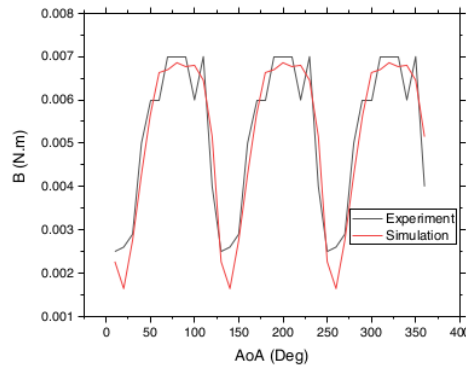Fig. 8 The turbine static torque measurement on the OWC prototype
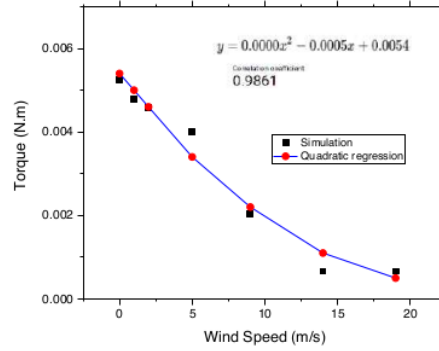

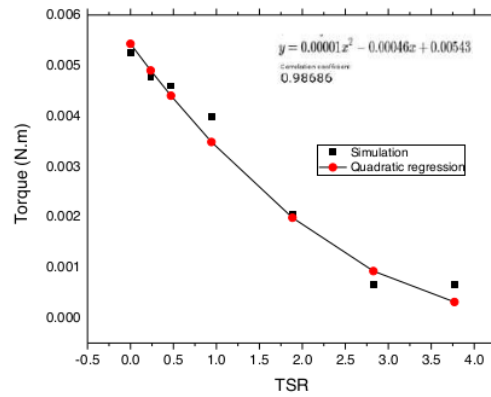Fig. 9 Rotor torque vs. AoA

Fig. 10 Turbine torque vs. airspeeds

Fig. 11 Rotor torque vs. wind velocity

Fig. 12 shows a graph of the correlation between the turbine speed (m/s) and airspeeds (m/s). A linear equation is obtained based on the prototype measurement data sampling as shown in Eq. (13), where Ws is wind speed (m/s), $\Theta = -345.603619236845$, $\Lambda = 396.2937800495123$, and $\Omega = 170.99764196071726$. R_T is the turbine rotor rotation (rpm), WS is the airspeeds in the OWC system (m/s). From Fig. 12, it appears that the fish-ridge turbine produces high turbine rotation at low airspeeds. This condition is due to the turbine's lightweight and the increased air pressure in the chamber OWC. In actual conditions, the turbine rotation speed is influenced by the turbine forming material.

$$R_T \ = \ \Theta + \ \Lambda \ (\text{Ws}) \ + \ \Omega \ (WS^2) \tag{13}$$
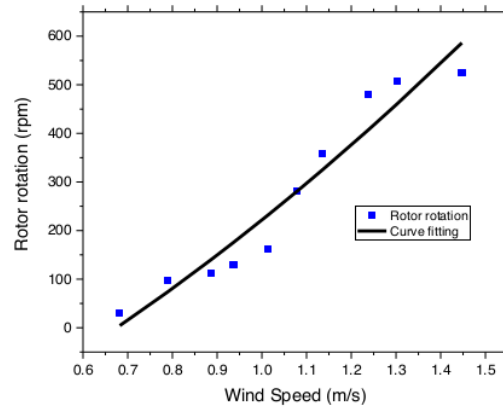
Fig. 12 Rotor rotation vs. airspeeds

3.3 Aerodinamik fish-ridge in OWC

Like the OWC chamber in actual conditions (Fig. 2), the water level inside the OWC chamber is determined by the water surface behavior outside the chamber. The chamber water surface has three different states; they are steady, high, and low. The steady-state is where there are no waves outside the chamber. The low-state is where the increased air pressure comes from inside the chamber area and then flows to the turbine then goes to the air outlet, called a compressed condition. The low-state is where the wave peak is at the negative peak so that high air pressure comes from the outlet to the turbine and is stuck in the chamber, which is called a decompressed condition. This condition is continuous during wave oscillation outside the chamber, while the turbine rotation continues in one direction under compressed conditions and calm conditions.

A CFD simulation of a fish-ridge turbine performance that depicts airspeeds and air pressure contours in the OWC system under compressed conditions is described in Fig. 19. In contrast, the decompressed state is represented in Figs. 15 and 16.

Fig. 13 shows a contour of airspeeds on a fish-ridge turbine under compressed conditions. At Θ=90 degrees, it appears that the airspeeds from the chamber have a slow rate. It was 0.127 m/s on the surface of the concave area of the A2 blade. The airspeeds in laminar form occur in the overlap area and towards the concave blade area of sections A1 and A3. This laminar form due to the significant pressure in the A2 concave area of the blades.

At Θ=60 degrees, turbulence begins to form in the A2 and A3 blades concave plane, increasing the wind flow rate in A2. When Θ=30 degrees, the turbulence-shaped flow becomes very significant with a speed of 1.1 m/s in the concave area of blade A1. The greater the turbulence flow at Θ=0 degrees. The overlap area with OR = 15% allows airflow in the laminar form to support the non-thrust blades have more thrust. This cycle occurs for each blade; therefore, this cycle is repeated for each of the blades.

Fig. 14 shows a contour of compressed air pressure on a fish-ridge turbine in an OWC system. At Θ=90 degrees, the immense pressure is 0.368Pa on the concave surface of A2 blades, while at
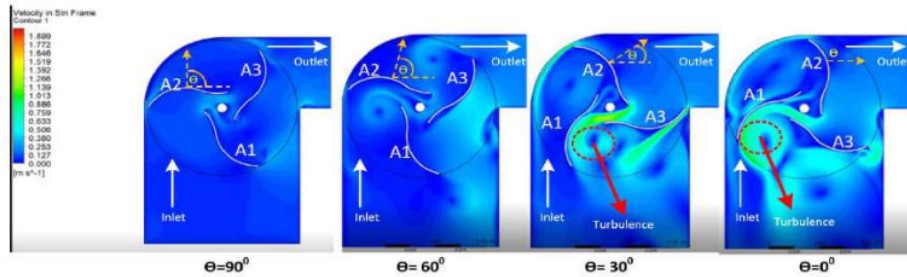
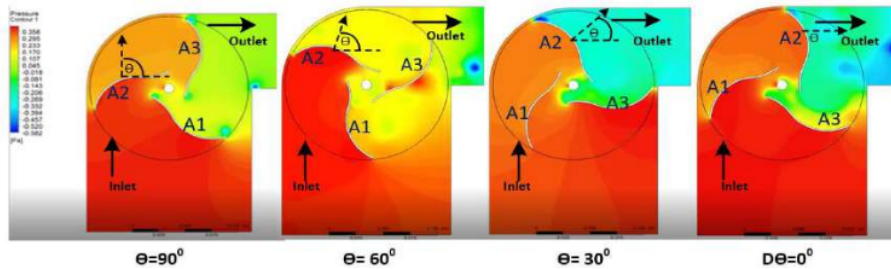Fig. 13 Airspeeds on turbine blades under compressed conditions

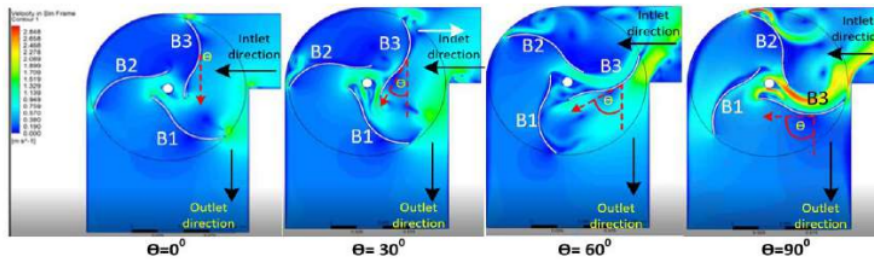Fig. 14 Air pressure on the turbine in the chamber under compressed conditions

Fig. 15 The contour of airspeeds distribution at decompressed conditions

low pressure, 0.045 Pa occurs on convex A3. At Θ=60 degrees, low pressure occurs on the concave and convex A3 parts of 0.107Pa at Θ=30 degrees, low pressure occurs at convex A2 and continues at Θ=0 degrees. This cycle occurs for each blade of the fish-ridge turbine.
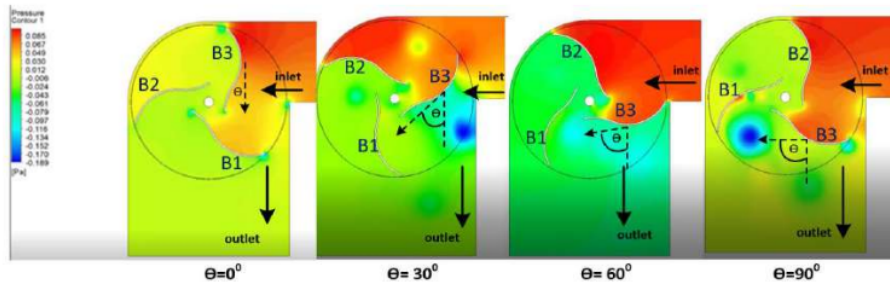
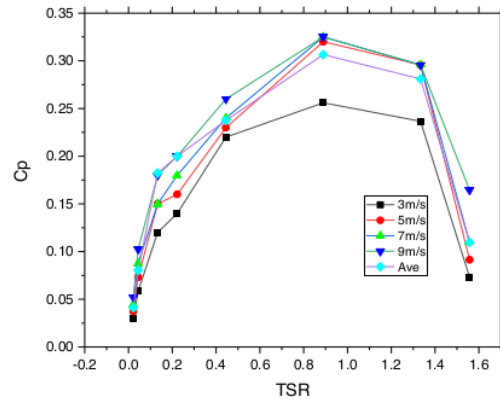Fig. 16 The contour of air pressure distribution at decompressed conditions

Fig. 17 Power coefficient vs. TSR at the compressed condition

From Figs. 13 and 14, it can be concluded that, in the distribution of wind flow, the fish-ridge turbine with OR=15% of the wind flow is continuously distributed. The fish-ridge turbine also proved that the aerodynamic drag of the turbine did not occur significantly. The shape of the OWC, which tends not to have free air space, makes air pressure isolated on one blade only, while the other blades experience low air pressure. In the compressed conditions based on Figs. 14 and 15, with varying airspeeds 3 m/s, 5 m/s, 7 m/s, 9 m/s in the fish-ridge turbine model in the compressed condition, we can draw a relationship of power coefficient (Cp) to TSR under compressed conditions as shown in Fig. 17.

The airspeed variation applied to the model appears that the maximum turbine efficiency reaches 30% at TSR=0.9, as shown in Fig. 17. These results prove that the implementation of the fish-ridge turbine in the OWC system produces better efficiency than applied to open spaces as has been done in (Song *et al*. 2013). Compared to the savonius study (Hassanzadeh and Mohammadnejad 2019),
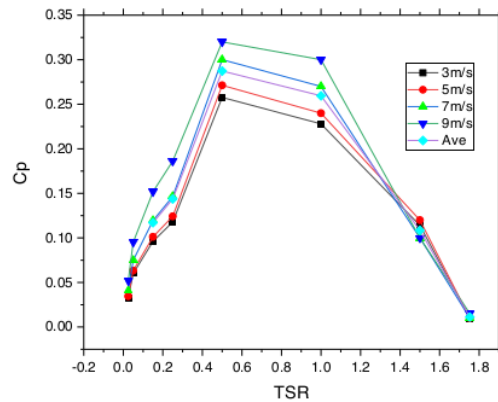
Fig. 18 Power coefficient vs. TSR at the decompressed condition

The fish-ridge turbine produces higher efficiency. In the OWC system, there is high air pressure due to the oscillation of the water surface in the chamber.

From Fig. 17, it appears that high compressed condition causes the turbine to extract energy in the TSR range between 0.8 to 1.2, meaning that the fish-ridge turbine experiences optimum efficiency at low waves (TSR=0.8) to high waves (TSR=1.2). This fact proves that the application of a fish-ridge turbine can work optimally at low to high waves.

Fig. 15 shows a contour of airspeeds on a fish-ridge turbine under decompressed conditions. The wind flow from the inlet to the turbine is not the same during the compressed conditions, so the wind flow contour analysis starts from Θ=0 degrees and ends at Θ=90 degrees.

When Θ=0 degrees, the high-speed wind flows on concave B1 and partially flows to the B2 blade through the overlap area in the form of laminar flow. At Θ=30 degrees, the wind flow increases on the blades of concave B1 and concave B2. At Θ=60 degrees, the laminar flow with a speed of 1,899 m/s is evenly distributed over the concave section of blade B3. A turbulent stream begins to appear at the convex end of the B2 blade. At Θ=90 degrees, the flow of laminar shape with a velocity of 2,848 m/s flows on concave B3, and the turbulence flow increases in the convex area of blade B2.

Fig. 16 shows a contour of decompressed air pressure in a fish-ridge turbine in an OWC system. Analysis of air pressure under decompressed conditions starts from Θ=0 degrees and ends at Θ=90 degrees. At Θ=0 degrees, high air pressure occurs in the concave area B1, while B2 and B3 experience low air pressure. At Θ=30 degrees, the air pressure in the concave area of B1 drops significantly, while the air pressure in the concave area of B3 becomes high. At Θ=60 degrees, the maximum air pressure occurs in the concave area of B3, up to Θ=90 degrees. This procedure is one duty cycle for each turbine.

Figs. 15 and 16 decompressed conditions with varying airspeeds, namely 3 m/s, 5 m/s, 7 m/s, and 9 m/s in the fish-ridge turbine model OWC decompressed system that the maximum efficiency of the turbine reaches 28% at TSR=0.6 (Fig. 18). this value is lower than in the compressed condition. However, at TSR=1.0, the turbine efficiency still came 26%, then plunged at TSR> 1.0.
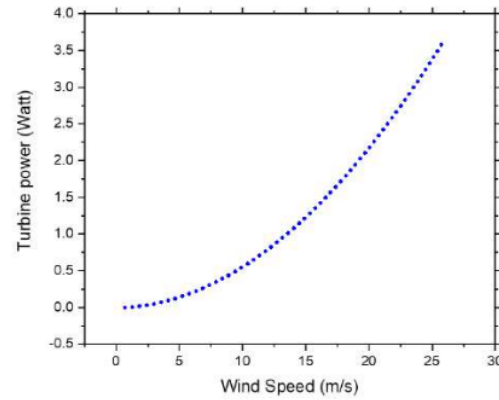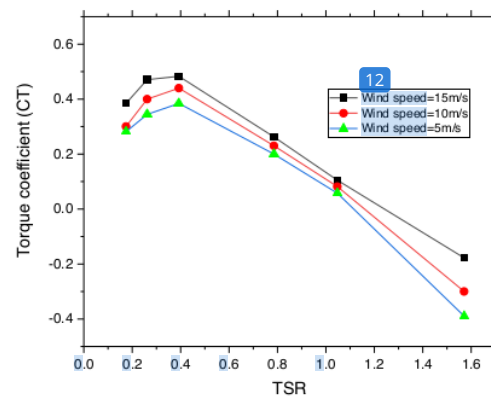
Fig. 19 Power turbine vs. airspeeds

Fig. 20 Torque vs. TSR

Compared to turbine efficiency under compressed conditions (Fig. 17), turbine efficiency under decompressed conditions (Fig. 18) is more sensitive at low airspeeds. Still, the TSR range and efficiency levels are minor than under compressed conditions.

From the above observations, it can be concluded that the aerodynamic behavior in compressed conditions involves maximum airspeeds of 1.90 m/s and air pressure of 0.36 Pa in the system. In comparison, in a decompressed condition, the maximum airspeed was 2.86 m/s with a maximum air pressure reaching 0.085 Pa., meaning that the turbine rotates more slowly but with enormous torque during the compressed condition. In contrast, when in the decompressed condition, the turbine rotates faster but with lower torque than under compressed conditions. The fish-ridge turbine in the OWC system absorbs wind energy into kinetic energy at faster rotation at low airspeeds. This condition is proof that fish-ridge has little aerodynamic resistance.

Using the simulation results from Table 3 by collecting the CFD data, the relationship between the airspeeds in the chamber and the power generated by the turbine is obtained, as shown Fig. 19. It appears that there is a fish-ridge turbine power which increases with increasing airspeeds on the turbine. Numerically, the relationship between the airspeeds and the turbine power generated is expressed in Eq. (14), where PT is the turbine power (watts), Ws is the wind speed or airspeeds in the OWC (m/s), Π = -0.005112414150319368, Γ = 0.0027620508076888735, Υ =0.005307706457862304. The torque coefficient of the turbine with variations in airspeeds shows in Fig. 20. The test results obtained a linear relationship with the airspeeds around the turbine, as in Fig. 20. It appears that in the variation of airspeeds in the OWC system, the peak torque coefficient of the fish-ridge turbine occurs at TSR = 0.3, then drops significantly at TSR> 0.4. We agree that the fish-ridge turbine in the OWC system is very easy to rotate at low speeds.

$$P_T \ = \ \Pi + \Gamma(W_S) \ + \ \Upsilon(W_S{}^2) \tag{14}$$

4. Conclusions

This article presents a fish-ridge turbine's performance results on an OWC system from an aerodynamic perspective regarding airspeeds and pressure for energy extraction. Our proposed design shows low-wind resistance. Fish-ridge turbine behavior in an OWC system at decompressed conditions is more sensitive than at compressed conditions. An Overlap ratio OR=15% causes a laminar flow from the turbine blades that do not directly thrust from the accident wind. The distribution of wind flow is evenly distributed on all turbine blades. In the compressed condition, the maximum efficiency of the fish-ridge turbine was 30% achieved at TSR 0.9.

In contrast, in the decompressed-condition, the maximum efficiency of the turbine was 28%. And it was achieved at TSR 0.6. We also found that the fish-ridge turbine is more sensitive to achieve maximum performance in the decompressed condition. The maximum torque coefficient of the turbine was 55% at TSR 0.3

Acknowledgments

References

Agbormbai, J. and Zhu, W. (2020), "Experimental study of the performance of a novel vertical-axiswind turbine", *Appl. Sci.*, **10**(8). https://doi.org/10.3390/APP10082902.

Bachtiar, I. K. (2019), "The Effect of Blade Overlap on The Performance of Savonius Wind Turbine", *Proceedings of the 2019 IEEE Conference on Energy Conversion (CENCON)*. IEEE, 236-239. doi: https://doi.org/10.1109/CENCON47160.2019.8974807.

Chao, M.A., Song, L. and Hang, M.Z. (2017), "Performance Study for A Novel Vertical Axis Wind Turbine based on Simulation Analysis", *Proceedings of the Networking, Sensing and Control (ICNSC), 2017 IEEE 14th International Conference on*. Calabria, Italy.

Chen, L., *et al.* (2016), "Wind tunnel investigation on the two- and three-blade Savonius rotor with central shaft at different gap ratio", *J. Renew. Sust. Energ.*, **8**(1). https://doi.org/10.1063/1.4940434.

Hassanzadeh, R. and Mohammadnejad, M. (2019), "Effects of inward and outward overlap ratios on the two-blade Savonius type of vertical axis wind turbine performance", *Int. J.Green Energy*, **16**(15), 1485-1496. https://doi.org/10.1080/15435075.2019.1671420.

Hiron, N., *et al.* (2019), "The Performance of a Three-blades Fish-ridge Turbine in an Oscillating Water Column System for Low Waves", *Proceedings of the 2019 International Conference on Sustainable Engineering and Creative Computing (ICSECC)*. IEEE.

Hiron, N., Andang, A. and Busaeri, N. (2019), "Investigation of Wireless Communication from Under Seawater to Open Air with Xbee Pro S2B Based on IEEE 802.15.4 (Case Study: West Java Pangandaran Offshore Indonesia)", *Adv. Intel. Syst. Comput.*, 672-681. https://doi.org/10.1007/978-3-030-02683-7_47.

Kang, C., *et al.* (2018), "Upstream flow control for the savonius rotor under various operation conditions", *Energies*, **11**(6), 1-20. https://doi.org/10.3390/en11061482.

Kavade, R.K. and Ghanegaonkar, P.M. (2020), "Effect of blade pitching on power coefficient of small-scale vertical axis wind turbine at different tip speed ratios", *Wind Eng.*, **44**(3), 313-324. https://doi.org/10.1177/0309524X19849841.

Langer, S. and Swanson, R.C. (2020), "On Boundary-Value Problems for RANS Equations and Two-Equation Turbulence Models", *J. Sci. Comput.*, **85**(1), 1-33. https://doi.org/10.1007/s10915-020-01323-9.

Lipian, M., Czapski, P. and Obidowski, D. (2020), "Fluid-structure interaction numerical analysis of a small, urban wind turbine blade", *Energies*, **13**(7), 1-15. https://doi.org/10.3390/en13071832.

Matoug, C., *et al.* (2020), "An hybrid approach for the comparison of VAWT and HAWT performances for floating offshore wind turbines", *J. Phys. Conference Series*, **1618**(3). https://doi.org/10.1088/1742-6596/1618/3/032026.

Morshed, K.N., *et al.* (2019), "Wind tunnel testing and numerical simulation on aerodynamic performance of a three-bladed Savonius wind turbine", *J. Appl. Fluid Mech.*, **12**(3), 819-829. https://doi.org/10.29252/jafm.12.03.29324.

Muneer, A., *et al.* (2015), "CFD analysis of a Savonius Vertical Axis Wind Turbine", *Energies*, **8**(4), 3013-3033. https://doi.org/10.3390/en8043013.

Rahman, M.M. (2020) "Introducing consistently formulated eddy-viscosity coefficient with spalart–allmaras model", *AIAA J.*, **58**(6), 2764-2769. https://doi.org/10.2514/1.J059118.

Shamsoddin, S. and Porté-Agel, F. (2020), "Effect of aspect ratio on vertical-axis wind turbine wakes", *J. Fluid Mech.*, **889**, 11-112. https://doi.org/10.1017/jfm.2020.93.

Sobczak, K., *et al.* (2020), "Numerical investigations of the savonius turbine with deformable blades", *Energies*, **13**(14). https://doi.org/10.3390/en13143717.

Song, L., Liu, H. and Yang, Z. (2016), "Orthogonal Analysis Based Performance Optimization for Vertical Axis Wind Turbine", *Math. Probl.. Eng.*, 334-339. http://dx.doi.org/10.1155/2016/6241360, Research.

Song, L., Liu, H.Z. and Yang, Z.X. (2015), "Performance comparison for savonius type wind turbines by numerical analysis approaches", *Proceedings of the International Conference on Advanced Mechatronic Systems, ICAMechS*, 2015-Octob.

Song, L.S., Ang, Z.Y. and Eng, R.D. (2013) ,"Performance and Structure Optimization for a New Type of Vertical Axis Wind Turbine", *Proceedings of the 2013 International Conference on Advanced Mechatronic Systems*. IEEE.

Yang, Z., *et al.* (2021), "Reynolds-Averaged Navier-Stokes Equations Describing Turbulent Flow and Heat Transfer Behavior for Supercritical Fluid", *J. Therm. Sci.*, **30**(1), 191-200. https://doi.org/10.1007/s11630-020-1339-6.

Yao, J., *et al.* (2019), "Parameter analysis of savonius hydraulic turbine considering the effect of reducing flow velocity", *Energies*, **13**(1). https://doi.org/10.3390/en13010024.

PL

Fish-ridge wind turbine aerodynamics characteristics in Oscillating Water Column (OWC) system

Smart-Green Technology in Electrical and Information Systems (ICSGTEIS), 2021
Publication

6   S. Li, Q. Li, J. Liang, P. Guo. "Investigation of the Transiting Test Method for the Aerodynamic Performance of Vertical Axis Wind Turbine Using Wind Generated by a Moving Vehicle", Experimental Techniques, 2021   <1%
Publication

7   studentsrepo.um.edu.my   <1%
Internet Source

8   Takahashi, Kazuki, and Mingcong Deng. "Nonlinear sensorless cooling control for a peltier actuated aluminum plate thermal system", Proceedings of the 2013 International Conference on Advanced Mechatronic Systems, 2013.   <1%
Publication

9   Submitted to Universitas Siliwangi   <1%
Student Paper

10   Zheng Li, Ruihua Han, Peifeng Gao, Caisheng Wang. "Analysis and implementation of a drag-type vertical-axis wind turbine for small distributed wind energy systems", Advances in Mechanical Engineering, 2019   <1%
Publication

11 Submitted to Cranfield University
Student Paper
<1%

12 mdpi-res.com
Internet Source
<1%

13 Sercan Yagmur, Faruk Kose, Sercan Dogan. "A study on performance and flow characteristics of single and double H-type Darrieus turbine for a hydro farm application", Energy Conversion and Management, 2021
Publication
<1%

14 opus.lib.uts.edu.au
Internet Source
<1%

15 res.mdpi.com
Internet Source
<1%

16 Ayse Simsek, Suleyman Teksin, Selahaddin Orhan Akansu, Yahya Erkan Akansu. "Performance analysis of Savonius wind turbines in different models", Wind Engineering, 2021
Publication
<1%

17 Can Kang, Wisdom Opare, Chen Pan, Ziwen Zou. "Upstream Flow Control for the Savonius Rotor under Various Operation Conditions", Energies, 2018
Publication
<1%

18   Esmaeel Fatahian, Farzad Ismail, Mohammad Hafifi Hafiz Ishak, Wei Shyang Chang. "An innovative deflector system for drag-type Savonius turbine using a rotating cylinder for performance improvement", Energy Conversion and Management, 2021
Publication   <1%

19   H.Y. Peng, M.N. Liu, H.J. Liu, K. Lin. "Optimization of twin vertical axis wind turbines through large eddy simulations and Taguchi method", Energy, 2021
Publication   <1%

20   Separated Flows and Jets, 1991.
Publication   <1%

21   Triyogi Yuwono, Gunawan Sakti, Fatowil Nur Aulia, Adi Chandra Wijaya. "Improving the performance of Savonius wind turbine by installation of a circular cylinder upstream of returning turbine blade", Alexandria Engineering Journal, 2020
Publication   <1%

22   hdl.handle.net
Internet Source   <1%

23   link.springer.com
Internet Source   <1%

24   mafiadoc.com
Internet Source   <1%

25	tethys-engineering.pnnl.gov Internet Source	<1 %
26	www.mdpi.com Internet Source	<1 %
27	www.tandfonline.com Internet Source	<1 %
28	"Contemporary Ideas on Ship Stability", Springer Science and Business Media LLC, 2019 Publication	<1 %
29	Thierry Villeneuve, Grégoire Winckelmans, Guy Dumas. "Increasing the efficiency of vertical-axis turbines through improved blade support structures", Renewable Energy, 2021 Publication	<1 %